

LIGHT PROPAGATION IN INHOMOGENEOUS UNIVERSES

III. DISTRIBUTIONS OF IMAGE SEPARATIONS

HUGO MARTEL¹, PREMANA PREMADI², AND RICHARD MATZNER^{3,4}

¹ Department of Astronomy, University of Texas, Austin, TX 78712

² Department of Astronomy & Bosscha Observatory, Bandung Institute of Technology, Indonesia

³ Center for Relativity, University of Texas, Austin, TX 78712

⁴ Department of Physics, University of Texas, Austin, TX 78712

ABSTRACT

Using an analytical model, we compute the distribution of image separations resulting from gravitational lensing of distant sources, for 7 *COBE*-normalized CDM models with various combinations of Ω_0 and λ_0 . Our model assumes that multiple imaging results from strong lensing by individual galaxies. We model galaxies as nonsingular isothermal spheres whose parameters are functions of the luminosity and morphological type, and take into account the finite angular size of the sources. Our model neglects the contribution of the background matter distribution to lensing, and assumes that lensing is entirely caused by galaxies. To test the validity of this assumption, we performed a series of ray-tracing experiments to study the effect of the background matter on the distribution of image separations. Our results are the following: (1) The presence of the background matter tends to increase the image separations produced by lensing galaxies, making the distributions of image separations wider. However, this effect is rather small, and independent of the cosmological model. (2) Simulations with galaxies and background matter often produce a secondary peak in the distribution of image separations at large separations. This peak does not appear when the background matter is excluded from the simulations. (3) The effect of the background matter on the magnification distribution is negligible in low density universes ($\Omega_0 = 0.2$) with small density contrast ($\sigma_8 = 0.4$), but becomes very important as Ω_0 and σ_8 increase, resulting in a significant widening of the distribution. (4) Multiple imaging is caused primarily by early-type galaxies (elliptical and S0's), with a negligible contribution from spiral galaxies. (5) Our analytical model, which has only 2 free parameters, is in good agreement with the results of ray-tracing experiments, successfully reproducing the distributions of image separations, and also the multiple-imaging probability, for all cosmological models considered. (6) The analytical model predicts that the distributions of image separations are virtually indistinguishable for flat, cosmological constant models with different values of Ω_0 . (7) For models with no cosmological constant, the distributions of image separations do depend upon Ω_0 , but this dependence is weak. We conclude that while the number of multiple-imaged sources can put strong constraints on the cosmological parameters, the distribution of image separations does not constrain the cosmological models in any significant way, and mostly provides constraints on the structure of the galaxies responsible for lensing.

Accepted for publication in *The Astrophysical Journal*

1. INTRODUCTION

The multiple imaging of distant source is the most spectacular manifestation of gravitational lensing. Since the discovery of the original binary quasar 0957+561 (Walsh, Carswell, & Weymann 1979), the number of multiply-imaged sources have been steadily growing, and at present 64 sources with multiple images have been identified (Kochanek et al. 1998)⁵. Multiple-image systems are characterized by their total magnification, image brightness ratio, and image separation. The distribution of these quantities, the image separation in particular, can be used to study the properties of the lenses, of the underlying cosmological background, and, to some extent, of the sources. A common approach for studying gravitational lensing consists of performing ray-tracing experiments, using a multiple lens-plane algorithm (Schneider, Ehlers, & Falco 1992, hereafter SEF). These experiments predict numerous properties of gravitational lenses that can be compared with observations to constrain the cosmological models. We have designed our own version of the multiple lens-plane algorithm (Premadi, Martel, & Matzner 1998, hereafter Paper I). This version includes the contributions to lensing caused by the distribution of background dark matter, as well as individual galaxies. We have used this algorithm to perform the largest cosmological parameter survey ever done in this field (Premadi et al. 2001, hereafter Paper II).

In Paper II, we introduced an analytical model for the distribution of image separations. This model successfully reproduced the least noisy of our numerically-generated distributions, the ones for which the number of cases was large enough to be statistically significant. The goal of this paper is to explore this analytical model in more detail, to investigate its properties, its accuracy, and the validity of the assumptions on which it is based.

Modeling the distribution of image separations analytically is not a new idea. In their seminal paper, Turner, Ostriker, & Gott (1984, hereafter TOG) studied the image separations resulting from galaxies modeled as point masses or singular isothermal spheres, in universes with density parameter $\Omega_0 = 0$ and $\Omega_0 = 1$. More recent studies include Hinshaw & Krauss (1987), Narayan & White (1988), Paczyński & Wambsganss (1989), Kochanek (1995), Porciani & Madau (2000), Keeton, Christlein, & Zabludoff (2000), Li & Ostriker (2001), Keeton (2001), and Takahashi & Chiba (2001). The main difference between these previous studies and our own is in the choice of galactic model. With the exception of Hinshaw & Krauss (1987), these studies only considered galactic models with singular density profiles, either point masses, singular isothermal spheres, or NFW halos (see Navarro, Frenk, & White 1996, 1997). We model galaxies as nonsingular isothermal spheres with a finite core. This is an important assumption that needs to be justified. Recent large N-body simulations of structure formation in CDM models predict that galaxies and clusters have a singular, or “cuspy,” density profile which approaches a power law $\rho \propto r^{-n}$ at the center, with the exponent n ranging from 1 to 1.5 (Cole & Lacey 1996; Navarro et al. 1996, 1997; Tormen, Bouchet, & White 1997; Fukushige & Makino 1997, 2001a, b; Moore et al. 1998, 1999; Huss, Jain, & Steinmetz 1999; Ghigna et al. 2000; Jing & Suto 2000; Klypin et al. 2000. See, however, Kravtsov et al. 1998). However, these results are in conflict with several observations. Dark-matter-dominated dwarf galaxies and low surface brightness galaxies exhibit rotation curves which imply mass profiles which are inconsistent with a singular shape, but are well fit by a mass profile with a central core (see reviews by Primack et al. 1998; Burkert & Silk 1999; and Shapiro, Iliev, & Raga 1999). At the other extreme, on the cluster scale, observations of strong gravitational lensing of background galaxies by foreground clusters indicate the presence of a finite-density core in the center of clusters (Tyson, Kochanski, & Dell’Antonio 1998). At the intermediate scale, HST observations of massive early-type galaxies (Lauer et al. 1995) reveal that these galaxies have brightness profiles that break from steep outer power laws to shallower inner cusps. The inner profiles, inside the break, remain singular, but the power-law exponents have a wide, bimodal distribution, ranging from $n = 0$ to $n = 2.5$ (Gebhardt et al. 1996), in conflict with numerical simulations.

This conflict between observations and simulations is a major challenge to the current CDM model of structure formation, and some authors have even claimed that the CDM model is ruled out. The most widely accepted viewpoint is that the observations are correct, and that the N-body simulations are in disagreement with observations because they are ignoring a crucial physical process. The two leading candidates for this physical process are gasdynamics (see, e.g. El-Zant, Shlosman, & Hoffman 2001) and self-interacting dark matter (Spergel & Steinhardt 2000), which both have the potential to eliminate the central cusp in the

⁵ See <http://cfa-www.harvard.edu/castles>

density profile and reconcile simulations with observations.

In this paper, we take the viewpoint that in the presence of such conflict, we should regard as “realistic” a galaxy model that is in good agreement with the observations, even if it might be in conflict with the simulations. Hence, we use a galaxy model (non-singular isothermal sphere) which has a finite-density core. This is what distinguishes this work from other analytical studies. Of all these previous studies, the one that most closely resembles our work is the study of Hinshaw & Krauss (1987), the only one that considers the effect of a finite-density core on the distribution of image separations. These authors model galaxies as nonsingular isothermal spheres which follow a Schechter luminosity function. We use the same assumption in this paper. Still, there are 5 important differences between this study and the one of Hinshaw & Krauss: (1) we consider different cosmological models, including in particular flat models with a nonzero cosmological constant, (2) our analytical model corrects the lensing cross section to account for the finite size of the source, (3) we include an observational selection effect, by discarding multiple images if the image separation is too small for the images to be resolved individually, either because the images overlap or the angular spacing between them is below the resolution limit of the observations, (4) while the study of Hinshaw & Krauss was purely analytical, we compare our analytical predictions with results of ray-tracing experiments, (5) we investigate the effect of the background matter on lensing by galaxies.

The remainder of this paper is organized as follows. In §2, we describe the cosmological models considered in this paper. In §3, we investigate the effect of the background matter on the distributions of image separations and magnifications. In §4, we describe our analytical model for the distributions of image separations. Results are presented in §5 and summarized in §6.

2. THE COSMOLOGICAL MODELS

In Paper II, we considered 43 different *COBE*-normalized Tilted Cold Dark Matter models. Each model was characterized by the value of the density parameter Ω_0 , cosmological constant λ_0 , Hubble constant H_0 , and rms density fluctuation σ_8 . The tilt n of the power spectrum was adjusted in order to reproduce the desired value of σ_8 for any particular combination of Ω_0 , λ_0 , and H_0 . We are considering the same models in this paper, and use, for our analytical calculations, the same galaxy distributions that were generated for the calculations presented in Paper II. As we will see in §3, our analytical model depends only on the intrinsic properties of galaxies, and not their level of clustering. Hence, the resulting separation distributions are independent of σ_8 , and galaxy distributions taken from models with different values of σ_8 can be combined. Furthermore, the analytical model turns out to be independent of H_0 . This reduces the 43 four-parameter models of Paper II to 7 two-parameter models. The values of the parameters Ω_0 and λ_0 for these 7 models are listed in the second and third columns of Table 1.

Table 1: The Cosmological Models

Model	Ω_0	λ_0	σ_8	% Ellipticals ^a	% S0's ^a	% Spirals ^a
O1	0.2	0.0	0.3 – 0.7	11 – 13	27 – 34	53 – 62
L1	0.2	0.8	0.6 – 1.0	12 – 14	32 – 35	51 – 56
O2	0.5	0.0	0.8 – 1.0	13 – 14	34 – 36	50 – 53
L2	0.5	0.5	0.8 – 1.0	13 – 14	34 – 36	51 – 53
O3	0.7	0.0	0.9 – 1.1	13 – 14	35 – 36	50 – 52
L3	0.7	0.3	0.9 – 1.1	13 – 14	35 – 36	50 – 52
E	1.0	0.0	0.9 – 1.3	13 – 14	35 – 36	49 – 51

^a Percentages are rounded to the nearest integer.

Strictly speaking, this reduction from 43 models to 7 models is not quite correct. The galaxy distributions actually depend upon σ_8 , but that dependence is indirect and quite weak. In the original algorithm of Jaroszyński (1991,1992), the morphological types of galaxies were chosen randomly. In Papers I and II, we improved the algorithm by choosing the morphological types according to the observed morphology-density relation (Dressler 1980; Postman & Geller 1984), locating more early-type galaxies and fewer spiral galaxies

in dense regions. Since the density contrast of dense regions depends directly upon σ_8 , the relative number of early-type and spiral galaxies varies with σ_8 , and this should affect the galaxy distributions. The last 4 columns of Table 1 list the range of values of σ_8 , and of the percentages of ellipticals, S0's, and spiral galaxies, respectively, for the various cosmological models. Varying the value of σ_8 does not affect dramatically the proportions of galaxies of various types. The largest fluctuations are for the model $\Omega_0 = 0.2$, $\lambda_0 = 0$, $H_0 = 75$, for which σ_8 varies from 0.3 to 0.7, and the corresponding fraction of spiral galaxies varies from 56% to 62%. We have compared distributions predicted by models differing only by the value of σ_8 , and found them to be nearly undistinguishable. Therefore, we are justified to combine models with different values of σ_8 .

3. THE EFFECT OF THE BACKGROUND MATTER

A crucial assumption of our analytical model is that gravitational lensing is essentially caused by individual galaxies, and that the effect of the background matter is unimportant and can be neglected. This is contrary to the widespread opinion that gravitational lensing by galaxies can be significantly affected by the presence of the background matter. This opinion is based primarily on the work of TOG. These authors calculated the effect of the background matter on lensing analytically, and provided formulae to correct the image separation and magnification produced by a galaxy for the presence of the background matter (TOG, eqs. [2.36] and [2.37]). To obtain this analytical result, they had to make 3 simplifying assumptions: (1) the galaxies are modeled as singular isothermal spheres, with a $\rho \propto r^{-2}$ density profile, (2) the background matter is approximated as a sheet of matter of constant surface density Σ and (3) the source is aligned with the lensing galaxy. While assumption (3) is probably of little consequence for the image separations,⁶ the other assumptions are not. A singular isothermal sphere has a density profile that is much steeper than the profiles obtained by numerical simulations, which are themselves steeper than the observed density profiles of galaxies and clusters. Also, a uniform sheet of constant surface density is a very crude representation of the actual structures that form out of Gaussian random noise initial conditions in a CDM universe. TOG, in their Appendix B, warn their readers that in the real universe, there would be overdense and underdense regions (“sheets” and “holes”) along the line of sight, and their effects would partly cancel out.

To estimate the effect of the background matter in the context of a CDM universe, we went back to the ray-tracing experiments presented in Paper II, which included the effects of both galaxies and background matter. We then modified our multiple lens-plane algorithm to take out the contribution from the background matter, and did 3 new series of experiments, for 3 different cosmological models: an open model ($\Omega_0 = 0.2$, $\lambda_0 = 0$, $H_0 = 75 \text{ km s}^{-1} \text{Mpc}^{-1}$, $\sigma_8 = 0.4$) a flat, cosmological constant model ($\Omega_0 = 0.2$, $\lambda_0 = 0.8$, $H_0 = 65 \text{ km s}^{-1} \text{Mpc}^{-1}$, $\sigma_8 = 0.8$) and an Einstein-de Sitter model ($\Omega_0 = 1$, $\lambda_0 = 0$, $H_0 = 65 \text{ km s}^{-1} \text{Mpc}^{-1}$, $\sigma_8 = 0.9$). In this section, we compare the results of the experiments with and without the contribution of the background matter included.

3.1. The Distribution of Image Separations

Figure 1 shows the distributions of image separations for the 3 cosmological models considered. The solid lines are the distributions obtained when the effect of galaxies and background matter are both included (these histograms are taken directly from Paper II). The dotted lines are the distributions obtained when only the effect of galaxies is included. All three panels show a similar trend: when only galaxies are included, the peaks of the distributions are higher, and the distributions are narrower. The presence of the background matter lowers the counts at separations $s \lesssim 2''$ and increases them at separations $s \gtrsim 2''$, producing a tail that extends to high separations. Notice that the secondary peak in the distribution at $s = 5''$ for the flat model (middle panel) disappear when the background matter is removed. We speculated in Paper II that this secondary peak, present for many cosmological models, resulted from the combined effect of galaxies and background matter. The results plotted in Figure 1 support this idea.

We computed the mean \bar{s} , standard deviation σ_s , and skewness of the distributions plotted in Figure 1. The results are listed in Table 2, where an \times in the second column indicates that the background matter

⁶ The image separation is actually independent of the position of the source in the absence of the background matter, for a singular isothermal sphere.

was included (\bar{s} and σ_s are in arc seconds; the skewness is dimensionless). The values of \bar{s} and σ_s are very similar among the 3 cases with background matter, and also among the 3 cases without. The presence of the background matter increases \bar{s} by about 10% and σ_s by about 15%. The skewness is definitely positive, and tends to increase when the background matter is included, because of the presence of the high-separation tail. These results are consistent with claims that the effect of the background matter on image separation is of order 20% or less (Bernstein & Fischer 1999; Romanowsky & Kochanek 1999). Keeton et al. (2000) showed that the dependence of the luminosity function on environment, which we neglect in this paper, decreases the proportion of high-mass galaxies relative to dwarfs in dense environments, and that this effect nearly cancels the effect of the background matter, making the distributions of image separations essentially independent of environment.

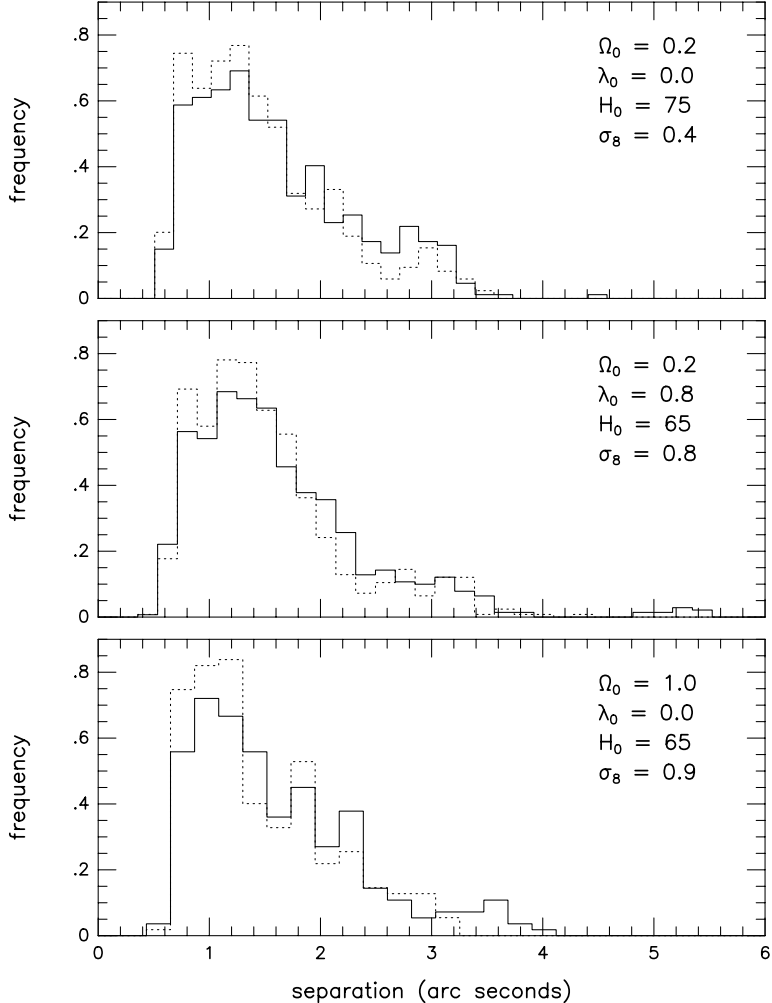


Fig. 1: Distribution of image separations in arc seconds for 3 different cosmological models. The solid lines show the distribution obtained when the presence of the background matter is taken into account. The dotted lines show the distribution obtained when the presence of the background matter is ignored. Both distributions were computed using ray-tracing experiments.

Figure 1 and Table 2 yield two important results concerning the distributions of image separations: (1) The effect of the background matter on the distributions of image separations produced by galaxies is essentially independent of the cosmological model. Not only do we observe the same trend in all panels of Figure 1, but the effect of the background matter is of the same order for all models. (2) The effect of

the background matter is far from spectacular. The only significant effect that might be observable is the high-separation tail. In any case, these results show that the effect of the background matter is small and it is not unreasonable to neglect it, as we do in our analytical model.

Table 2: Statistics of the Distributions of Image Separations

Model (Ω_0, λ_0)	Background	\bar{s}	σ_s	Skewness
(0.2,0.0)	×	1.60	0.71	0.81 ± 0.17
(0.2,0.0)	—	1.47	0.64	0.99 ± 0.17
(0.2,0.8)	×	1.64	0.80	1.67 ± 0.14
(0.2,0.8)	—	1.52	0.67	1.22 ± 0.15
(1.0,0.0)	×	1.61	0.74	1.03 ± 0.24
(1.0,0.0)	—	1.46	0.62	0.83 ± 0.24

3.2. The Magnification Distribution

Using the calculations presented in this section, we estimate the effect of the background matter on the distribution of magnifications, even though this is not the main focus of this paper, which is concerned only with the distribution of image separations. We include this subsection for completeness. Figure 2 shows the distributions of magnifications for the 3 cosmological models considered. As in Figure 1, the solid curves show the results when both galaxies and background matter are included (they are also taken directly from Paper II), while the dotted curves show the distributions when only galaxies are included. There is a major difference between these results and the ones shown in Figure 1. While the effect of the background matter on the distribution of image separations is model-independent, the effect on the magnification distribution strongly depends on the cosmological model. In the top panel, for the open model, the two curves are nearly undistinguishable, indicating that the effect of the background matter is totally negligible. For the two other models, the presence of the background matter results in a widening of the distribution, which is moderate for the flat model (middle panel) but very important for the Einstein-de Sitter model (bottom panel).

Since the focus of this paper is on the distribution of image separations, we will postpone a detailed study of the magnification distribution to another paper. But let us speculate on the origin of the phenomenon revealed by Figure 2. In the filled-beam approximation, which we use in these calculations, the background matter would have absolutely no effect on lensing if it was uniform. The density fluctuations in the background matter are responsible for deflecting light, and the magnitude of these fluctuations are measured by the parameter σ_8 . Thus, we expect the effect of the background matter to be larger for the flat and Einstein-de Sitter models, which have $\sigma_8 = 0.8$ and 0.9 respectively, than for the open model, which has $\sigma_8 = 0.4$. This is indeed the case, but it does not explain why the effect of the background matter for the open model is totally negligible. We speculate that the explanation resides in the structure formation process. In cosmological model such as CDM, structures form hierarchically through mergers. As the universe evolves, clusters become more massive, voids become deeper, and the actual number of voids and clusters decreases. The value of σ_8 measures the level of clustering, and is therefore related to the stage that this hierarchical formation process has reached. In models with small σ_8 , not only the density fluctuations are small compared with model with higher σ_8 , but in addition the overdense and underdense regions have a smaller physical size (since the hierarchical merging process is not as well-advanced), and therefore there should be a very large number of overdense and underdense regions along any line of sight, leading to a near-perfect cancellation. A model with larger σ_8 has fewer clusters and voids along the line of sight, and a cancellation is less likely. This idea certainly deserves more investigation.

Finally, let us point out that the difference between the flat model (middle panel) and the Einstein-de Sitter model (bottom panel) results primarily from the different values of Ω_0 . The Einstein-de Sitter model has nearly 5 times more background matter than the flat model.

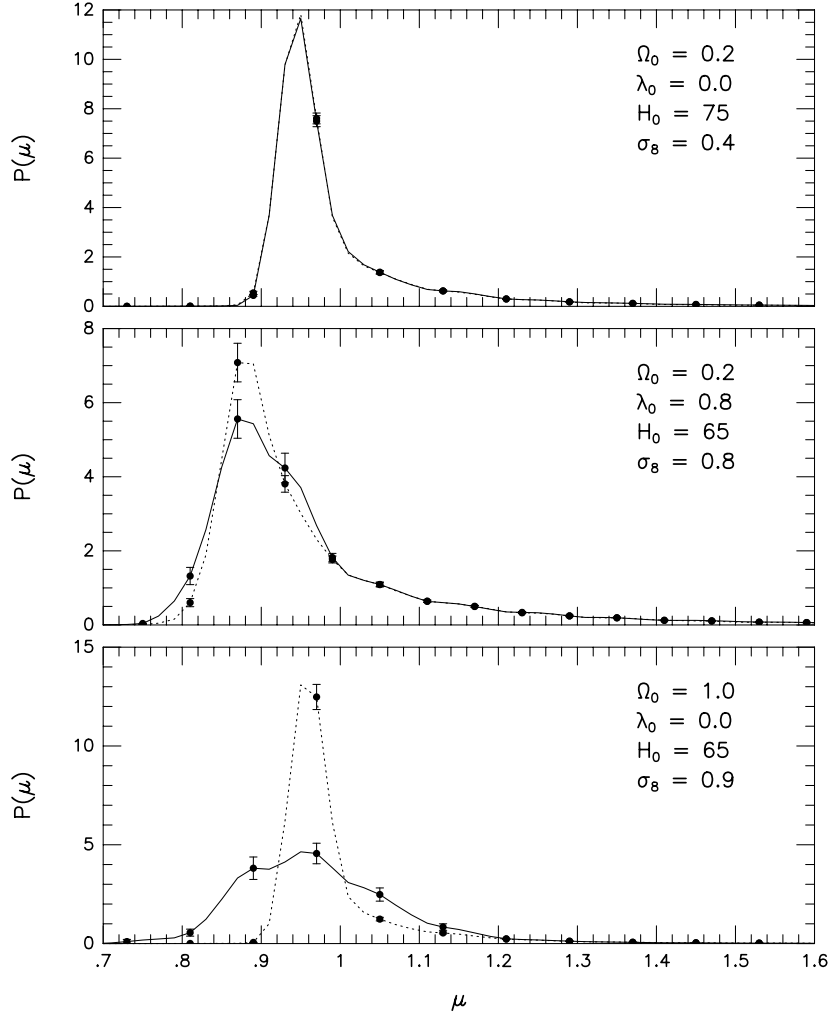


Fig. 2: Distribution of magnifications for 3 different cosmological models. The solid curves show the distribution obtained when the presence of the background matter is taken into account. The dotted curves show the distribution obtained when the presence of the background matter is ignored. Error bars indicate 1σ uncertainties. Both distributions were computed using ray-tracing experiments.

4. ANALYTICAL MODEL OF THE DISTRIBUTION OF IMAGE SEPARATIONS

In this section, we describe the various assumptions on which our analytical model is based. The validity of these assumptions is discussed in §6 below.

4.1. The Galactic Models

We assume that the galaxy luminosities follow a Schechter luminosity function,

$$n(L)dL = \frac{n_*}{L_*} \left(\frac{L}{L_*} \right)^\alpha e^{-L/L_*} dL, \quad (1)$$

where $n(L)$ is the number density of galaxies per unit luminosity. We use the values $\alpha = -1.10$, $n_* = 0.0156 h^3 \text{Mpc}^{-3}$, and $L_* = 1.3 \times 10^{10} h^{-2} L_\odot$, where h is the Hubble constant in units of $100 \text{ km s}^{-1} \text{Mpc}^{-1}$

(Efstathiou, Ellis, & Peterson 1988). We also introduce a minimum luminosity $L_{\min} = 0.01L_*$ to prevent the total number of galaxies from diverging. The corresponding present number density and luminosity density are $n_0 = 0.0808 h^3 \text{Mpc}^{-3}$ and $j_0 = 2.13 \times 10^8 h L_\odot \text{Mpc}^{-3}$, respectively. We adopt the galaxy models described by Jaroszyński (1991, 1992). Each galaxy is modeled by a truncated, non-singular isothermal sphere, whose parameters depend upon the galaxy luminosity and morphological type. The projected surface density of each galaxy is given by

$$\sigma(r) = \frac{v^2}{4G(r^2 + r_c^2)^{1/2}}, \quad (2)$$

where r is the projected distance from the center. The parameters r_c and v are the core radius and rotation velocity, respectively, and are given by

$$r_c = r_{c0} \left(\frac{L}{L_*} \right), \quad (3)$$

$$v = v_0 \left(\frac{L}{L_*} \right)^\gamma, \quad (4)$$

where the parameters r_{c0} , v_0 , and γ are given in Table 3. We use a Monte-Carlo method to generate for each galaxy a luminosity $L \geq L_{\min}$, with a probability $P(L)$ proportional to $n(L)$.

Table 3: Galaxy Parameters

Type	r_{c0} ($h^{-1}\text{kpc}$)	v_0 (km s^{-1})	γ
Elliptical	0.1	390	0.250
S0	0.1	357	0.250
Spiral	1.0	190	0.381

4.2 The Analytical Model

To compute analytically the distribution of image separations, we make the following assumptions:

(1) Lensing is entirely caused by galaxies; we ignore the effect of the background matter. Based on the results presented in §3.1, this is a reasonable assumption.

(2) Each galaxy acts as if it was alone; we ignore the tidal effects of nearby galaxies, and the possibility of lensing events involving several galaxies. We can justify this assumption as follows. Lensing is produced by the most massive galaxies, which are also the most luminous. These galaxies are quite rare. Equation (1), with our assumed cutoff $L_{\min} = 0.01L_*$ predicts that only 2% of galaxies have a luminosity $L > L_*$. Hence, a galaxy massive enough to produce multiple images is likely to be surrounded by much less massive galaxies, whose tidal influence will be at most a small perturbation.

(3) Galaxies are modeled as nonsingular isothermal spheres, as described in §4.1.

With these assumptions, the problem is reduced to studying lensing by isolated, nonsingular isothermal spheres. The geometry of this problem is illustrated in Figure 3. The optical axis goes through the observer and the center of the lensing galaxy, r_c is the core radius of the galaxy, η is the distance between the source and the optical axis, and the quantities D_L , D_{LS} , and D_S are the angular diameter distances between observer and lens, lens and source, and observer and source, respectively. All properties of this lensing system can be expressed as functions of dimensionless ratios between r_c , η , D_L , D_{LS} , and D_S , and the dimensionless ratio v/c , where r_c and v are given by equations (3) and (4), respectively, and c is the speed of light.

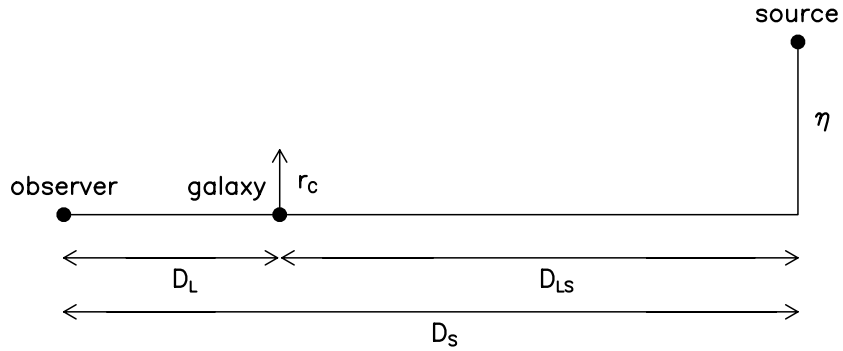


Fig. 3: The lensing geometry: the dots indicate the location of the observer, lensing galaxy, and source. r_c is the core radius of the galaxy, and η is the distance between the source and the optical axis. The angular diameter distances D_L , D_{LS} , and D_s are also indicated.

(4) We neglect any spatial correlation between the sources and the lens. The probability that a particular galaxy will produce multiple images is then proportional to its angular cross section for multiple imaging. However, we shall include a correction to this cross section to account for the finite angular size of the sources (see below).

(5) To build a realistic distribution, we must impose limits on the smallest possible image separation that allows individual images to be resolved. Throughout this paper, we assume that sources have an angular diameter $2\alpha_S = 1''$, where α_S is the angular radius of the source. The smallest possible image separation is then of order $\alpha_S = 0.5''$. To illustrate this, we reproduce in Figure 4 a numerically-generated double image, taken from Paper II (Fig. 13c in that paper). The brightness ratio between the two images is very high, and the total magnification is not much larger than unity. This double image has about the same size as the source, and the image separation, measured between image centers, is therefore of order half the source diameter. However, the gap between the images is very small and might be difficult to resolve observationally. To take this selection effect into account, we introduce a free parameter $f > 1$, and we assume that at separations $s < \alpha_S$ the individual images can never be resolved, that at separations $s > f\alpha_S$ they can always be resolved, and that at separations $\alpha_S < s < f\alpha_S$ they can sometimes be resolved, with a probability that varies linearly from 0 to 1 between $s = \alpha_S$ and $s = f\alpha_S$. The probability of “resolvability” $P(s)$ is therefore given by

$$P(s) = \begin{cases} 0, & s < \alpha_S; \\ (s - \alpha_S)/\alpha_S(f - 1), & \alpha_S < s < f\alpha_S; \\ 1, & s > f\alpha_S. \end{cases} \quad (5)$$

Throughout this paper, we assume $\alpha_S = 0.5''$ and $f = 2$.

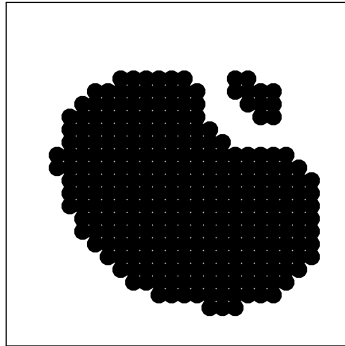


Fig. 4: Double image with low magnification and high brightness ratio. The image separation, measured between image centers, is of order the source angular radius. This figure is reproduced from Paper II.

Gravitational lensing by isolated, nonsingular isothermal spheres is an important problem, for which several analytical results have been derived (Dyer 1984; Hinshaw & Krauss 1987; Blandford & Kochanek 1987; Kochanek & Blandford 1987). We can directly apply these results to our analytical model. For each galaxy, we introduce a length scale ξ_0 , defined by

$$\xi_0 = 2\pi \left(\frac{v}{c}\right)^2 \frac{D_L D_{LS}}{D_S} \quad (6)$$

(SEF, eq. [8.34a], with $v = \sqrt{2}\sigma_v$). We use this parameter to rescale the core radius and the source position, as follows,

$$x_c = r_c/\xi_0, \quad y = \eta/\xi_0. \quad (7)$$

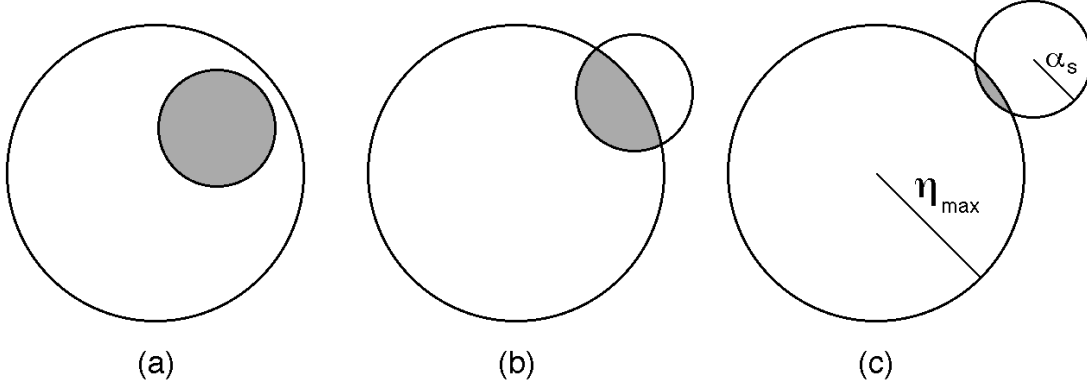


Fig. 5: Cross section for multiple imaging. The large and small circles represent the cross section and the source, respectively. The gray area indicates the part of the source that produces multiple images. η_{\max}/D_S and α are angular radii.

We will refer to x_c as the *scaled core radius*. We also define, for $x_c < 1$, a critical radius $y_r = (1 - x_c^{2/3})^{3/2}$. The nonsingular isothermal sphere has the following properties (SEF, §12.2.3): (1) If $x_c \geq 1$, the source has only one image. (2) If $x_c < 1$ the source has one image if $y \geq y_r$, and 3 images if $y < y_r$. Hence, each lens which satisfies the condition $x_c < 1$ has an angular cross section for multiple imaging $\sigma_{\text{m.i.}}$ given by

$$\sigma_{\text{m.i.}} = \pi \left(\frac{\eta_{\max}}{D_S} \right)^2 = \pi \left(\frac{y_r \xi_0}{D_S} \right)^2. \quad (8)$$

This expression is valid only for point sources. If the sources have a finite size, as we assume in our model, part of the source might be located inside the cross section even if the center of the source is not. This is illustrated in Figure 5, for 3 different locations of the source. In each panel, the gray area indicates the fraction of the source that can produce multiple images. We define the *effective* cross section $\sigma_{\text{m.i.}}^{\text{eff}}$ as

$$\sigma_{\text{m.i.}}^{\text{eff}} = \pi \left(\frac{\eta_{\max}}{D_S} + \zeta \alpha_S \right)^2 = \pi \left(\frac{y_r \xi_0}{D_S} + \zeta \alpha_S \right)^2, \quad (9)$$

where ζ is a tunable parameter. In principle, we should use $\zeta = 1$, since overlap occurs whenever the angular separation between the center of the source and the optical axis is less than $\eta_{\max}/D_S + \alpha_S$. However, if $\eta/D_S \lesssim \eta_{\max}/D_S + \alpha_S$, only a very small fraction of the source overlaps with the cross section given by equation (8), as Figure 5c shows. Only that part of the source will form multiple images, and these images will be very faint, possibly too faint to be resolved by observers, and also by ray-tracing experiments.⁷

⁷ In Paper II, we discarded from the analysis any image composed of less than 5 light rays, corresponding to a magnification less than 0.026.

We introduce the parameter ζ to take this selection effect into account. We found that $\zeta = 0.5$ is a good compromise, and leads to results that are in good agreement with the results of Paper II (see §5.1 below).

If a galaxy modeled as a nonsingular isothermal sphere produces multiple images (that is, 3 images), the angular separation s between the two outermost images depends upon the source position η , and has a maximum value given by

$$s = \frac{2\xi_0}{D_L} (1 - x_c^2)^{1/2}. \quad (10)$$

Hinshaw & Krauss (1987), and Cheng & Krauss (1999) showed that the dependence of s on η is weak. Following the suggestion made by SEF (p. 396), we will assume that whenever multiple images occur, the image separation is equal to this maximum value. We can then compute the distribution of image separations by including all galaxies which satisfy the condition $x_c < 1$. We give to each galaxy j a weight w_j equal to

$$w_j = \frac{(\sigma_{\text{m.i.}}^{\text{eff}})_j P(s_j)}{C(z_j)}. \quad (11)$$

where s_j is the image separation produced by galaxy j according to equation (10), $P(s_j)$ and $(\sigma_{\text{m.i.}}^{\text{eff}})_j$ are given by equations (5) and (9), respectively, and the redshift-dependent quantity $C(z)$ is the solid angle on the sky at redshift z that our sample of galaxies covers. This factor is given by $C(z) = [L_{\text{box}}/(1+z)/D_L(z)]^2$, where $L_{\text{box}} = 128$ Mpc is the comoving size of the computational volume in which the galaxy sample was generated (see Paper II). The probability that a random source will have resolvable multiple images is then given by adding up all the weights,

$$P_{\text{m.i.}} = \sum_{\text{all } j} w_j. \quad (12)$$

4.3. Contributions of the Various Galaxy Types

Before computing the actual distributions of image separations, we first estimate the relative contributions of high-mass and low-mass galaxies, and of the various morphological types. The usual assumption is that more massive galaxies produce larger image separations, and for galaxies modeled as singular isothermal spheres, this is certainly true. For galaxies with a finite core, this is only true up to a point. In equation (10), $\xi_0 \propto v^2 \propto L^{2\gamma}$, and therefore in the limit $x_c \ll 1$, the image separation increases with L . However, combining equations (3), (4), (6), and (7), we get $x_c \propto r_c/v^2 \propto L^{1-2\gamma}$. Since $\gamma < 1/2$ for all morphological types (see Table 3), x_c increases with L . Eventually, the factor $(1 - x_c^2)^{1/2}$ in equation (10) dominates, and the image separation decreases, until $x_c = 1$ and all images merge. Hence, there are two characteristic luminosities in this problem: the luminosity L_s for which the image separation s is maximum, and the luminosity L_1 , larger than L_s , for which $x_c = 1$ and only one image is produced (of course, L_s and L_1 are functions of the galaxy and source redshifts, the morphological type, and the cosmological model through the dependences on D_L , D_{LS} , D_S , and γ). To illustrate this, we plot in Figure 6 the image separation produced by a lensing galaxy at redshift $z_L = 0.3$, in a universe with $\Omega_0 = 0.3$, $\lambda_0 = 0.7$, $H_0 = 70 \text{ km s}^{-1} \text{Mpc}^{-1}$ (as usual, we assume a source redshift $z_S = 3$). The top panel shows the image separations produced by a spiral galaxy. The separation increases with L and reaches a maximum for $L = L_s$, then, the effect of the finite core radius becomes important, and the separation decreases until $L = L_1$ and the images merge together. The bottom panel shows the image separation produced by a S0 galaxy. The core radius is much smaller, and this pushes the values of L_s and L_1 off the right edge of the plot, at very large values of L/L_* .

If $L_1 < L_{\text{min}}$, the cutoff of the luminosity function, multiple images cannot be produced. To find out when this situation occurs, we reexpress the first of equations (7) as

$$x_c = \frac{r_c c^2 / 2\pi v^2 R_0}{D_L D_{LS} / D_S R_0}, \quad (13)$$

where $R_0 \equiv c/H_0$ is the Hubble radius. We have isolated in the numerator and denominator the dependences upon the galactic model and the cosmological model, respectively (the dependences of r_c and R_0 upon H_0 cancel out in the numerator). The denominator of equation (13) is plotted, versus the redshift z_L of the

lensing galaxy, in Figure 7 (solid curves) for the various cosmological models. Multiple imaging can only occur if $x_c < 1$, or equivalently, if the numerator in equation (13) is smaller than the denominator. Since $\gamma < 1/2$, r_c/v^2 is an increasing function of L , and takes its smallest value for $L = L_{\min}$, which was set to $0.01L_*$ in our simulations. The dotted lines in Figure 7 shows the resulting minimum values of the numerator of equation (13) for the various morphological types. Multiple imaging can only occur when the solid curve is above the dotted line, in which cases $L_1 > L_{\min}$, and $x_c < 1$ for all galaxies in the interval $[L_{\min}, L_1]$. As we see, early-type galaxies located at almost any redshift can produce multiple images as long as their luminosities are low enough. Spiral galaxies located too close to the observer, $z_L \lesssim 0.05$, or too close to the source, $z_L \gtrsim 2.0 - 2.4$, cannot produce multiple images.⁸ Of course, this is a consequence of our assumed galactic model, which is only an approximation. We do not expect spiral galaxies to follow rigorously equation (3), and spiral galaxies at low redshift can produce multiple images if their core radii happen to significantly smaller than our model assumes. A spectacular example is the quadruple-image lens Q2237, which is caused by a lensing spiral galaxy located at redshift $z_L = 0.04$.

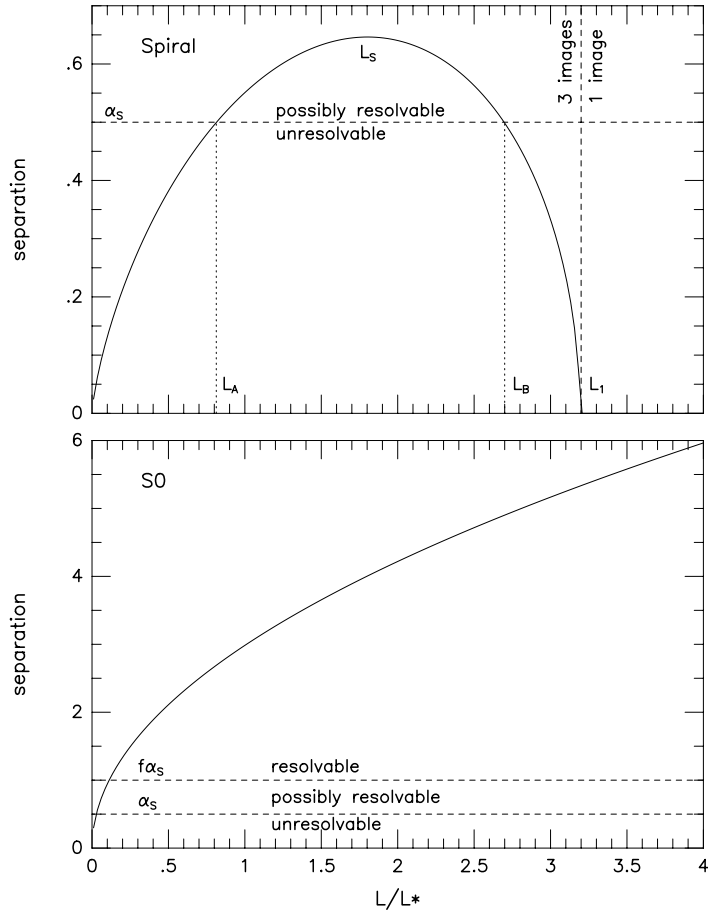


Fig. 6: Image separation versus galaxy luminosity, for a lensing spiral galaxy (top panel) and a S0 galaxy (bottom panel) located at redshift $z = 0.3$, in a universe with $\Omega_0 = 0.3$, $\lambda_0 = 0.7$, $H_0 = 70 \text{ km s}^{-1} \text{Mpc}^{-1}$ (solid curves). The horizontal dashed lines indicate the transitions between the various “resolvability” cases described by equation (5). The vertical dash line, defined by $x_c = 1$, indicates the transition from 3 images to 1. Lensing produces 3 images if $L < L_1$, and these images can be resolved individually if $L_A < L < L_B$. L_s is the luminosity for which the separation is maximum. In the bottom panel, $L_A = 0.03$ is near the origin; L_s , L_B , and L_1 are off the right edge of the plot.

⁸ This result depends on the particular choice we made for the luminosity cutoff L_{\min} , but notice that $(r_c/v^2)_{\min} \propto L_{\min}^{1-2\gamma}$ is a weakly-varying function of L_{\min} .

Even if a galaxy can produce multiple images, these images might blend together and be unresolvable if the image separation is too small. Our model assumes that images with angular separations less than $\alpha_S = 0.5''$ cannot be resolved individually. The luminosity L_s for which the image separation is maximum is a very complicated function, but with some simplifying approximations we can obtain a crude estimate of the maximum image separation that each type of galaxies can produce, as follows. Using equations (6) and (7), we rewrite equation (10) as

$$s = \frac{2}{D_L} \left[4\pi^2 \left(\frac{v}{c} \right)^4 \frac{D_L^2 D_{LS}^2}{D_S^2} - r_c^2 \right]^{1/2}. \quad (14)$$

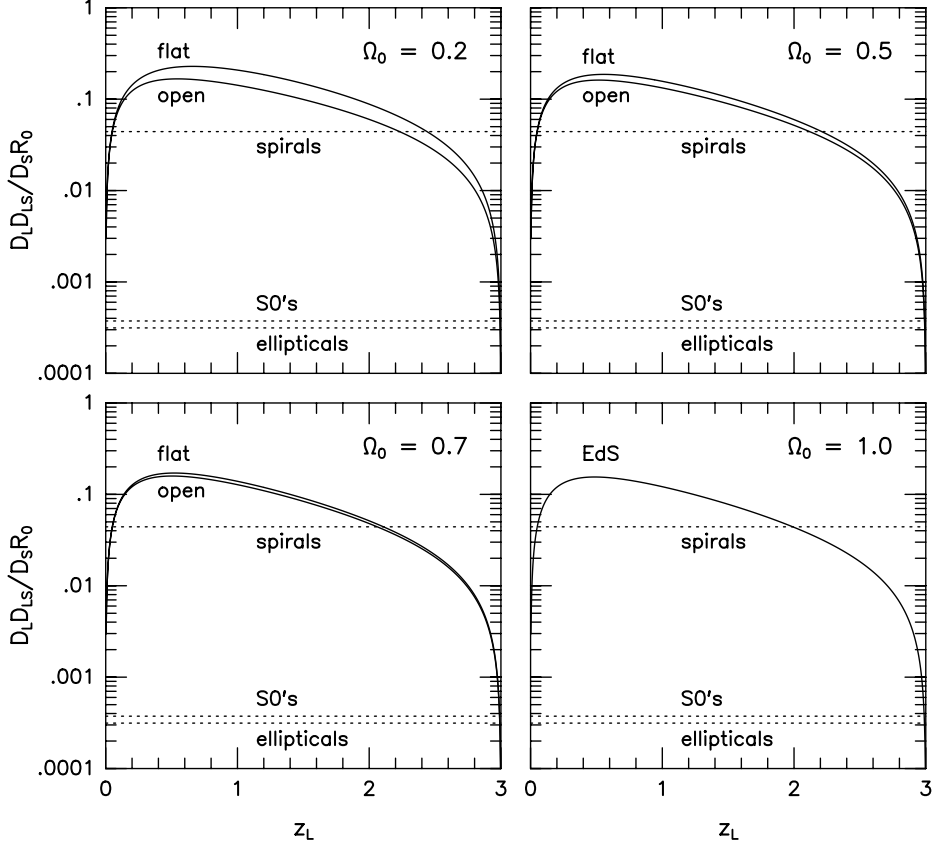


Fig. 7: Dimensionless ratio $D_L D_{LS} / D_S R_0$ versus lens redshift z_L , for source located at $z_s = 3$ (solid curves). The values of Ω_0 are indicated in each panels. The curves labeled “flat” correspond to $\Omega_0 + \lambda_0 = 1$ models and the ones labeled “open” correspond to $\lambda_0 = 0$ models. The dotted lines show the minimum value of the numerator of equation (13), for each morphological type.

Over most redshifts z_L of interest (that is, not too close to either the observer or the source), the quantities D_L and $D_L D_{LS} / D_S$ are not very sensitive to the redshift or the cosmological parameters (see Fig. 7 of this paper and Fig. 5 of Paper II). In this crude treatment, we can approximate them as constant. We set $D_L \sim 0.3R_0$ and $D_L D_{LS} / D_S \sim 0.2R_0$. We also eliminate r_c and v using equations (3) and (4). Equation (14) reduces to

$$s = \frac{20}{3} \left[0.16\pi^2 \left(\frac{v_0}{c} \right)^4 \left(\frac{L}{L_*} \right)^{4\gamma} - \frac{r_{c0}^2}{R_0^2} \left(\frac{L}{L_*} \right)^2 \right]^{1/2}. \quad (15)$$

This equation depends only upon the galactic model. To find the maximum separation, we differentiate equation (15) relative to L , set $ds/dL = 0$ and solve for L . We get

$$\frac{L}{L_*} = \left(\frac{r_{c0}^2}{0.32\pi^2 R_0^2 \gamma} \right)^{1/(4\gamma-2)} \left(\frac{v_0}{c} \right)^{-2/(2\gamma-1)}. \quad (16)$$

We eliminate L/L_* in equation (15) using equation (16). After some algebra, we get

$$s_{\max} = \frac{20}{3} \left(\frac{r_{c0}}{R_0} \right)^{2\gamma/(2\gamma-1)} \left(\frac{c^4}{0.32\pi^2 \gamma v_0^4} \right)^{1/(4\gamma-2)} \left(\frac{1}{2\gamma} - 1 \right)^{1/2}. \quad (17)$$

This equation predicts $s_{\max} = 93.2''$, $65.5''$, and $0.8''$ for elliptical, S0, and spiral galaxies, respectively. Of course, arc-minute separations like $93.2''$ or $65.5''$ are totally unrealistic. Just like we use a minimum luminosity L_{\min} in the luminosity function, there should be a maximum luminosity L_{\max} above which the luminosity function is no longer valid. Equation (16) gives $L/L_* = 2000$, 1400 , and 3.2 for elliptical, S0, and spiral galaxies, respectively. The first two numbers are of course absurd. If we choose, say, $L_{\max} = 3L_*$ for all morphological types and substitute this value in equation (15), we still get $s_{\max} = 5.1''$, $4.2''$, and $0.8''$ for elliptical, S0, and spiral galaxies, respectively. Clearly, early-type galaxies totally dominate the distribution of image separations. Spiral galaxies, with their smaller masses and much larger core radii, can at best produce image separations that are merely 60% larger than the threshold of resolvability ($s = 0.5''$).

Going back to Figure 6, we indicated on each panel the regions where individual images are resolvable ($P[s] = 1$), unresolvable ($P[s] = 0$), or possibly resolvable ($0 < P[s] < 1$), according to equation (5). For the spiral galaxy (top panel), we identify the following regimes: $L_{\min} < L < L_A$: 3 unresolvable images; $L_A < L < L_B$: 3 resolvable images; $L_B < L < L_1$: 3 unresolvable images; $L > L_1$: 1 image. Here L_A and L_B are the values of L for which $s = \alpha_S$. For the S0 galaxy, the value of L_A is near the origin, at $L_A \sim 0.03L_*$, and the value of L_B is off the right edge of the plot.

These results indicate that, in our model, most spiral galaxies responsible for multiple imaging have *intermediate* luminosities (or masses). High-luminosity spiral galaxies have large core radii that prevent them from producing multiple images, while low-luminosity spiral galaxies produce images with small separations, which blend together and are not resolvable individually. For early-type galaxies, the effect of the core radius enters only for values of L_* that are unrealistically large. Hence, early-type galaxies can always produce multiple images, unless they are too close to the source or the observer. Notice that the cross section for multiple imaging still favors lenses at intermediate redshifts.

In this discussion, we have expressed the image separation in terms of the luminosity L of the lensing galaxy, and not its mass M . Of course, for real galaxies, L is a monotonically increasing function of M , and therefore all the above statements could be rephrased in terms of the mass. However, our galactic models are defined in terms of the luminosity (eq. [1]–[4]). The reason is that the mass of an isothermal sphere (singular or nonsingular) diverges, unless a cutoff radius r_{\max} is introduced in the model. We actually used a cutoff radius r_{\max} in Papers I and II, but for the analytical model presented in this paper, a cutoff radius is unnecessary. Because the galactic models have a circularly symmetric projected surface density on the lens plane, lensing depends only on the total mass inside a cylinder of radius equal to the impact parameter on the lens plane. In the limit $r_{\max} \gg r_c$, this mass is finite and depends only on $r_c(L)$, $v(L)$, and the impact parameter. Hence, as long as the edge of each galaxy on the lens plane lies outside its critical curve, the value of r_{\max} , and consequently the value of the mass M , are irrelevant.

5. RESULTS

5.1. Multiple-Imaging Probability

Using equation (12), we computed the multiple-imaging probability $P_{\text{m.i.}}$ for the 7 models considered in this paper. The results are listed in the second column of Table 4. For comparison, we list in the third column of Table 4 the values obtained in Paper II, using ray-tracing experiments. The results are comparable for all models. The largest difference (19%) occurs for the Einstein-de Sitter model E, but this is precisely the model for which the ray-tracing value is most uncertain. These numbers validate our particular choice of $\zeta = 0.5$ in equation (9). We experimented with the value of ζ , and found that $\zeta = 0$ produced analytical values of $P_{\text{m.i.}}$ that were too small by a factor of 2–2.5 compared with the ray-tracing values, while $\zeta = 1$ produced values that were too large by a factor of 1.5.

Table 4: Multiple-Imaging Probability

Model	Analytical	Ray-tracing
O1	0.0023	0.0027
L1	0.0090	0.0086
O2	0.0026	0.0028
L2	0.0044	0.0043
O3	0.0025	0.0022
L3	0.0033	0.0031
E	0.0023	0.0019

The analytical results listed in the second column of Table 4 are exact. The numerical results listed in the third column are based on ray-tracing experiments, and are therefore approximate. It is difficult to estimate the uncertainty on these values, and a detailed error analysis of the ray-tracing experiments is beyond the scope of this paper (for details on how these numbers were obtained, we refer the reader to Paper II). We estimate that the uncertainties range from 15% to 25%, which is large enough to reconcile the experiments with the analytical model.

5.2. Distributions of Image Separations

5.2.1. Analytical Model vs. Ray-Tracing Experiments

In Figure 8, we compare the the distributions of image separations predicted by the analytical model (dotted lines) to the ones obtained in Paper II using ray-tracing experiments (solid lines), for the models O1, L1, and E. The agreement is excellent for model E (bottom panel). The large peaks at $s = 1.9''$ and $s = 2.3''$ in the ray-tracing distributions are statistical fluctuations. The agreement is quite good for model L1 (middle panel). The model overestimates the number of cases with $s < 1.2''$ and underestimates the number of cases in the range $1.2'' < s < 2.3''$ relative to the ray-tracing experiments. These experiments take the effect of the background matter into account, and this tends to shift separations to higher values. The agreement is not particularly good for model O1 (top panel), where the ray-tracing experiments produce a large deficit in the range $0.5'' < s < 1.2''$, and a large excess in the range $2.2'' < s < 3.2''$ relative to the analytical model. But between these features, the analytical model reproduces the ray-tracing results fairly well.

A strange feature that we reported in Paper II was the presence of a secondary peak at large separations. We clearly see this peak at $s \sim 5.2''$ in the middle panel, and we could also argue that the excesses predicted by the ray-tracing experiments at $s = 3.6''$ in the bottom panel and $2.2'' < s < 3.2''$ in the top panel are manifestations of the same phenomenon. As we showed in §3, this secondary peak appears to be caused by the background matter, in a way that remains to be explained. The poor agreement between the analytical model and the simulations for model O1 (top panel), would then be caused by the particularly large height of this secondary peak.

It is worth pointing out that for a given source size and source redshift, our analytical model has only two free parameters: f (eq. [5]) and ζ (eq. [9]). With the particular combination $f = 2$ and $\zeta = 0.5$, the model reproduces the distributions of image separations for 3 very different cosmological models, and also reproduces the multiple-imaging probabilities shown in Table 4 for 7 different cosmological models. That a 2-parameter model can satisfy so many constraints supports the notion that this model is accurate and based on assumptions that are sound.⁹

⁹ Actually, it only shows that assumptions (1), (2), (4), and (5) in §4.2 are sound. The analytical model and the ray-tracing simulations both assume the same galactic models, and therefore assumption (3), that these galactic models are correct, is neither supported nor invalidated by the comparison.

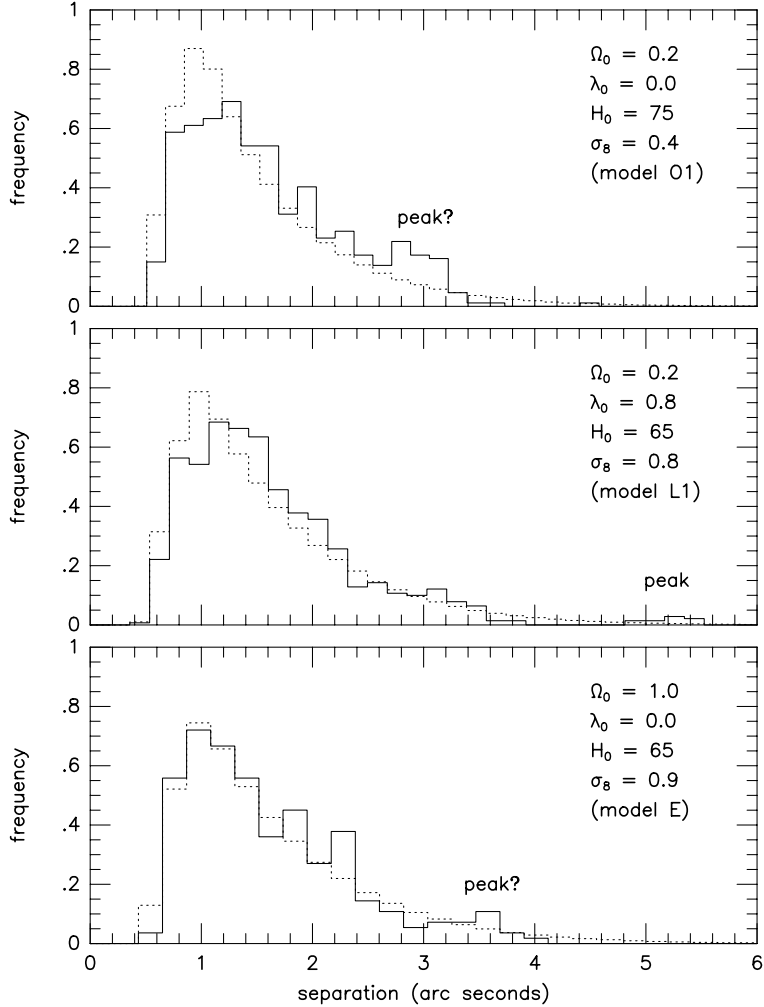


Fig. 8: Distribution of image separations in arc seconds, computed using ray-tracing experiments (solid lines) and using the analytical model presented in this paper (dotted lines). *Top*, model O1 ($\Omega_0 = 0.2$, $\lambda_0 = 0.0$, $H_0 = 75 \text{ km s}^{-1} \text{Mpc}^{-1}$, $\sigma_8 = 0.4$); *middle*, model L1 ($\Omega_0 = 0.2$, $\lambda_0 = 0.8$, $H_0 = 65 \text{ km s}^{-1} \text{Mpc}^{-1}$, $\sigma_8 = 0.8$); *bottom*, model E ($\Omega_0 = 1.0$, $\lambda_0 = 0.0$, $H_0 = 65 \text{ km s}^{-1} \text{Mpc}^{-1}$, $\sigma_8 = 0.9$). The locations or possible locations of secondary peaks are indicated.

5.2.2. Dependence upon the Cosmological Model

We plot the distributions of the scaled core radii x_c , critical radii y_r , and image separations s in Figures 9 and 10. Since our galaxy distributions, taken from Paper II, contained over 100,000 galaxies per model, with luminosities distributed according to equation (1), these curves are essentially *exact* predictions of the analytical model. In Figure 9, we compare models E (solid curves) and O1 (dotted curves), which are both matter-dominated ($\lambda_0 = 0$), while in Figure 10 we compare models E (solid curves) and L1 (dotted curves), which are both flat ($\Omega_0 + \lambda_0 = 1$).

The top panels of Figures 9 and 10 show bimodal distributions, with most values of x_c being in the range $\sim [0, 0.04]$ for early-type galaxies and $\sim [0.3, 1]$ for spirals galaxies. We excluded values of x_c larger than unity, since they do not result in multiple images. The concentration of the values of x_c near zero for early-type galaxies implies that, in our model, these galaxies behave nearly as *singular* isothermal spheres,

with the presence of a finite-density core having little effect. For spiral galaxies, the effect of the finite core can be very important, and even prevent the formation of multiple images (when $x_c > 1$). Early-type galaxies produce larger image separations than spirals: not only the factor ξ_0 in equation (10) is about 4 times larger for early-types than spirals (at a given luminosity), but in addition the factor $(1 - x_c^2)^{1/2}$, which is always near unity for early-type galaxies, can be quite lower for spirals. The observational selection effect described by equation (5) then becomes very important. As Table 1 shows, our galaxy distributions contain similar numbers of early-types and spiral galaxies, and the requirement $x_c < 1$ for multiple imaging only eliminate a small fraction of the spirals. However, the condition given by equation (5) eliminates about 50% of the early-type galaxies, but 95% of the spiral galaxies. In other words, only one of every 20 spiral galaxies can produce images that is sufficiently separated to be resolved individually. Hence, we expect early-type galaxies to dominate the distribution of image separations, with a negligible contribution from spiral galaxies.

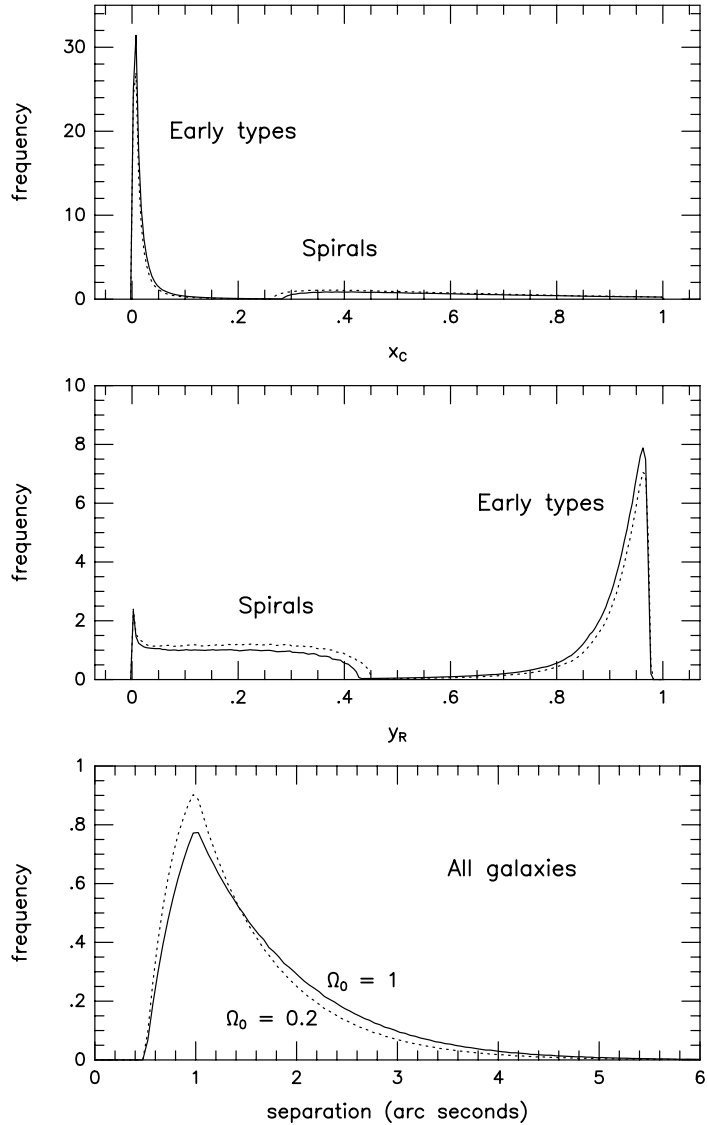


Fig. 9: *Top*, distribution of values of $x_c = r_c/\xi_0$; *middle*, distribution of values of $y_r = (1 - x_c^2)^{1/2}$; *bottom*, distribution of image separations in arc seconds. The solid and dotted curves correspond to the $\Omega_0 = 1, \lambda_0 = 0$ model and $\Omega_0 = 0.2, \lambda_0 = 0$ model, respectively. Only galaxies capable of producing multiple images ($x_c < 1$) are included.

The second panels of Figures 9 and 10 show the distributions of the values of y_r . The bimodality of the x_c distributions results in the distributions of y_r being also bimodal, with the values being concentrated near $y_r = 1$ for early-type galaxies and spread between 0 and 0.4 for spiral galaxies. Since the cross section for multiple-imaging scales like y_r^2 , this reinforces even more the dominance of early-type galaxies over spirals.

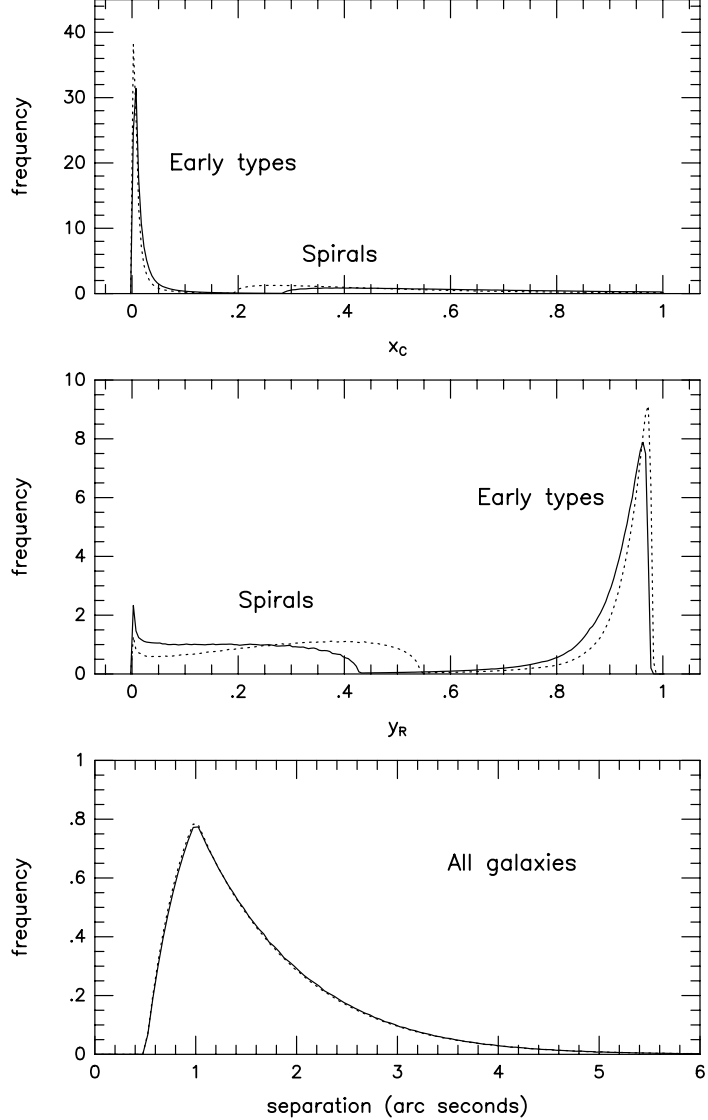


Fig. 10: Same as Figure 9, except that the dotted curves now correspond to the $\Omega_0 = 0.2$, $\lambda_0 = 0.8$ model. The two curves in the bottom panel are essentially undistinguishable.

The bottom panels of Figures 9 and 10 show the distributions of image separations predicted by our analytical model. These distributions were obtained by computing the image separation for all galaxies using equation (10), and ascribing to each separation a statistical weight w given by equation (11). Figure 9 shows that for matter-dominated models ($\lambda_0 = 0$), the distribution depends upon the density parameter. As Ω_0 increases, the peak of the distribution is lowered, and the high-separation tail extends to larger values. The intermediate models O2 and O3 follow this trend. For clarity, we did not include them in Figure 9. Figure 10 shows that for flat models ($\Omega_0 + \lambda_0 = 1$), the distribution does not depend upon the density parameter. Indeed the distributions for the E and L1 models, and for the intermediate models L2 and L3 (not plotted) are nearly indistinguishable, *even though the distributions of values of x_c and y_r are clearly different*, as the

top and middle panels of Figure 10 show. These differences are actually much more pronounced than the corresponding ones for the matter-dominated models (top and middle panels of Fig. 9).

To explain these surprising results, consider first the central panels of Figures 9 and 10, which show the distributions of the values of y_r . Early-type galaxies have significantly larger values of y_r than spirals. Since the cross section $\sigma_{\text{m.i.}}$ is proportional to y_r^2 , early-type galaxies dominate, and we can neglect, to a very good approximation, the presence of spiral galaxies. The top panels of Figures 9 and 10 then show that the values of x_c for early-type galaxies are much smaller than unity. Making the approximation $x_c \approx 0$, $y_r = (1 - x_c^{2/3})^{3/2} \approx 1$, the expressions for the image separation and the multiple-imaging cross section, equations (10) and (11), reduce to

$$s \approx 4\pi \left(\frac{v}{c}\right)^2 \frac{D_{LS}}{D_S}, \quad (18)$$

$$\sigma_{\text{m.i.}} \approx 4\pi^3 \left(\frac{v}{c}\right)^4 \left(\frac{D_L D_{LS}}{D_S^2}\right)^2, \quad (19)$$

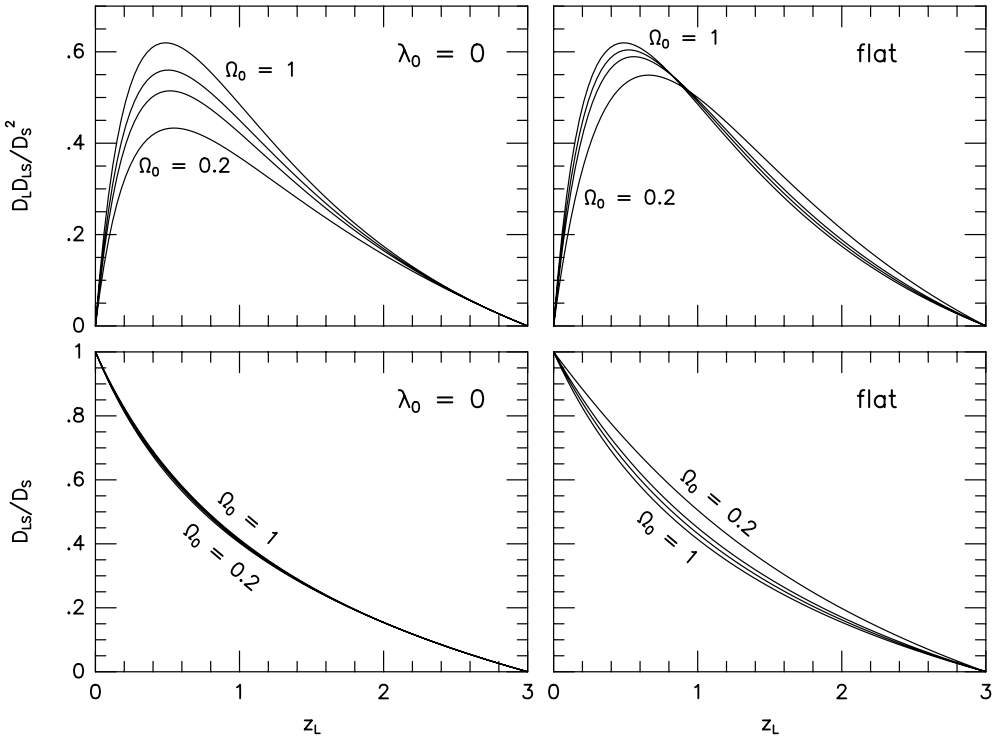


Fig. 11: Dimensionless angular diameter distance ratios $D_L D_{LS} / D_S^2$ (top panels) and D_{LS} / D_S (bottom panels) versus lens redshift z_L , for sources located at $z_S = 3$. Left panels: matter-dominated models ($\lambda_0 = 0$). Right panels: flat models ($\Omega_0 + \lambda_0 = 1$). The four curves on each panel correspond to $\Omega_0 = 0.2, 0.5, 0.7$, and 1 .

where, in equation (19), we also neglected the effect of the source size. These expressions depend upon the cosmological parameters only through the dimensionless distance ratios D_{LS} / D_S and $D_L D_{LS} / D_S^2$. These two ratios are plotted versus the lens redshift z_L in Figure 11. Using this figure, we can attempt to interpret the results shown in Figures 9 and 10. Consider first the matter dominated models (that is, Fig. 9 and left panels in Fig. 11). The ratio D_{LS} / D_S is essentially independent of Ω_0 . The ratio $D_L D_{LS} / D_S^2$, which determines the cross section, decreases with decreasing Ω_0 . The lensing probability is then reduced for smaller Ω_0 , but this effect alone could not affect the distributions shown in Figure 9, which are normalized. Notice, however, that the sensitivity of $D_L D_{LS} / D_S^2$ upon variations of Ω_0 depends on the galaxy redshift z_L . Near $z_L = 0.5$, where $D_L D_{LS} / D_S^2$ is maximum, $D_L D_{LS} / D_S^2$ decreases quite rapidly with decreasing Ω_0 ,

while at redshifts $z_L > 1.5$ the effect is much weaker. Looking now at the bottom left panel of Figure 11, we see that galaxies located at redshift $z_L \sim 0.5$ tend to produce larger image separations than galaxies located at redshifts $z_L > 1.5$.¹⁰ Hence, the reduction in cross section $\sigma_{\text{m.i.}}$ resulting from a reduction of Ω_0 affects large separations more than small separations, explaining the effect we see in the bottom panel of Figure 9.

The situation for the flat models (Fig. 10 and right panels in Fig. 11) is significantly more complicated. First, there is an inversion of the relationship between $D_L D_{LS} / D_S^2$ and Ω_0 . At redshifts $z_L > 0.9$, $D_L D_{LS} / D_S^2$ actually increases with decreasing Ω_0 , and this should reinforce the effect of favoring small separation angles over large ones. However, as Ω_0 decreases, the ratio D_{LS} / D_S increases, resulting in larger separations. These two effects clearly act in opposite directions. There is one additional complication: since all image separations increase with decreasing Ω_0 , several cases with small image separations will be pushed above the threshold of resolvability α_S (see eq. [5]). As Figure 10 shows, these various effect conspire to produce distributions of image separations that are essentially independent of Ω_0 .

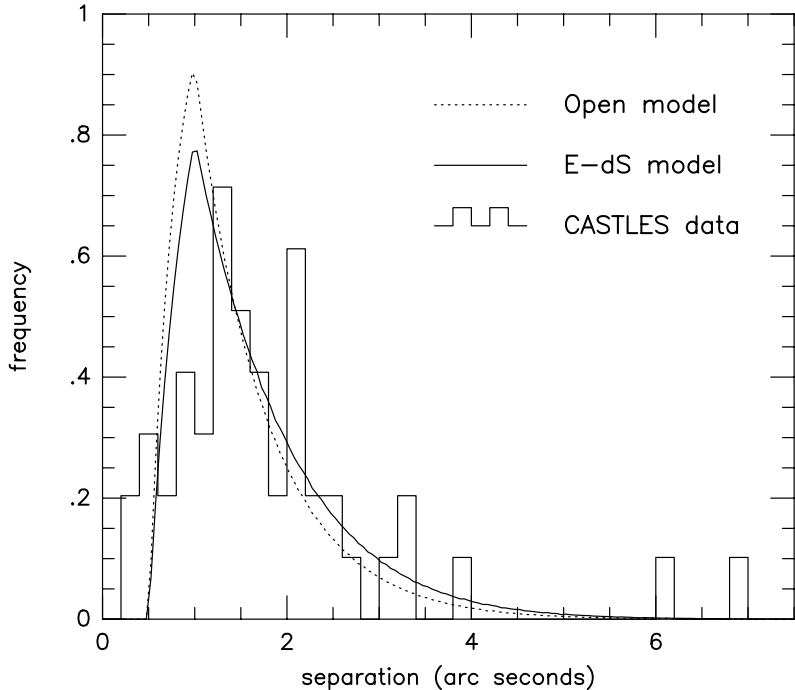


Fig. 12: Distributions of image separations for the $\Omega_0 = 0.2$, $\lambda_0 = 0$ model (open model, dotted curve) and $\Omega_0 = 1$, $\lambda_0 = 0$ model (Einstein-de Sitter model, solid curve). The histogram shows the distribution of observed gravitational lenses, based on the CASTLES database. The bins have a width of $0.2''$.

5.2.3. Comparison with Observations

In Figure 12, we reproduce the distributions of image separations plotted in the bottom panel of Figure 9 (solid and dotted curves). The histogram shows the observed distribution of image separations for 49 known gravitational lenses, taken from the CASTLES database¹¹ (Kochanek et al. 1998). The overall agreement between the models and the observations is quite good. The 3 main differences are (1) the peaks of the distributions are located at $s = 1''$ for the models, and $s = 1.3''$ for the observations, (2) there are lenses with separations $s < 0.5''$ in the observations, but not in the models, and (3) two known lenses have separations $s > 6''$, in conflict with the model, which predicts that such cases are extremely rare. Points (1) and (2) are clearly a consequence of equation (5), and the fact that our analytical model assumes a constant

¹⁰ But we must keep in mind that the separation does not depend only on the ratio D_{LS} / D_S , but also on the ratio v/c , which has a wide distribution.

¹¹ The CASTLES database is a web site which lists all information about known gravitational lenses, obtained from several published surveys performed by numerous authors.

source size. The rise of the distribution of image separations at $s = 0.5''$ would certainly be less steep if we used instead a distribution of source sizes, and also a distribution of source redshifts. Point (3) is very interesting. There are currently no observed lenses with image separations in the range $4'' < s < 6''$, but there are two lenses with separation $s > 6''$, Q0957+561 (e.g. Young et al. 1980) and RX J0912+4529 (Muñoz et al. 2001). In both cases it is believed that the large image separations result from the presence of the cluster in which the lens is located. Such large separations are inconsistent with our analytical model which ignores the presence of the background matter, but consistent with our ray-tracing experiments when these experiments take the background matter into account. Could these lenses with $s > 6''$ constitute the secondary peak seen in the middle panels of Figures 1 and 8? This is an exciting possibility, but clearly we need more data in order to test this hypothesis. The main conclusion we draw from Figure 12 is that the analytical model is in good agreement with the observations, for all cosmological models considered. A much larger number of observed lenses would be required in order to rule out the model, and an even larger number would be necessary to distinguish between the various cosmological models.

6. DISCUSSION

In this section, we review some of the assumptions of the model, and discuss their validity.

6.1. The Galactic Models

Our galactic models (§4.1) assume that lenses can be approximated as nonsingular isothermal spheres with a finite core. While observations of dwarf galaxies and clusters of galaxies indicate the presence of a flat, constant-density core, HST observations of nearby massive galaxies indicate that these objects also have a core, but the density profile inside these cores is still singular (or “cuspy”). The power-law exponents vary from 0 (flat core) to 2.5 (steeper than isothermal) with a bimodal distribution showing peaks at 0.8 and 2 (Gebhardt et al. 1996). For galaxies located in the lower end (exponents less than 1), our models can be regarded as a fairly reasonable approximation, in any case much better than the commonly used isothermal approximation. For galaxies in the upper end, our model is of course inappropriate. However, Gebhardt et al. (1996) show that there is a strong correlation between mass and density profile. The most massive galaxies, which are likely to be responsible for lensing, are the ones with the flattest density cores.

In a recent paper, Rusin & Ma (2001) argue that the absence of a detectable third image in lens systems rules out shallow profiles. At first sight, this seems to argue against profiles with a central core, though in the limit of a small core radius, these profiles reduce to an isothermal profile. The lack of detectable odd images rules out large regions of shallow profiles for the inner several kiloparsecs of galaxy mass distribution. In our galactic models, the core radii are given by $r_c = r_{c0}L/L_*$ [eq. (3)] where r_{c0} is $1.0h^{-1}$ kpc for spirals and $0.1h^{-1}$ kpc for early types, as indicated in Table 3. Therefore, only spiral galaxies with luminosities significantly larger than L_* have a core radius of several kiloparsecs, and such galaxies are exponentially rare. In other words, Rusin & Ma (2001) rule out the existence of cores that are much larger than the ones we consider.

There are other possible explanations for the absence of the third image. First, this image tends to be very close to the optical axis, and might be hidden behind the lens itself. Unless the lens is transparent, such image could not be seen.¹² Also, the third image is usually highly demagnified, and might be too faint to be seen. Finally, two images would appear as a single image if their angular separation is below the resolution limit. In Paper II, we performed a very large number of ray-tracing experiments, using exactly the same galaxy profiles as in this paper. We obtained 10,728 double-image systems, and only 126 triple-image systems (also, a negligible fraction of the Einstein rings we produced had a central spot). Hence, the paucity of triple-image systems is not inconsistent with our assumed galactic model. The simulations presented in Paper II had a finite numerical resolution, and an image could not be detected if it was demagnified by a factor of order 40 or more. We conclude that in these simulations most third images were indeed demagnified by a factor of more than 40. Such large demagnifications result from the fact that our assumed core radii are small, indeed significantly smaller than the ones ruled out by Rusin & Ma.

¹² Notice that the images studied by Rusin & Ma were obtained at radio wavelengths, and lenses should be transparent at these wavelengths.

The relationships between the galaxy parameters are complex, and the models described in §4 are only approximate. In particular, there is probably no one-to-one correspondence between core radius, luminosity, and rotation velocity for real galaxies. Also, our model assumes spherically symmetric lenses which follow a Schechter luminosity function. In the real world, lenses are not spherical, and the luminosity function is more complex than a Schechter form (see, in particular, Keeton et al. 2000).

In any case, it is very important to keep in mind what the goal of this paper is. Image separations can in principle tell us about either the nature of the lenses or the cosmological model. In this paper, we consider only the latter. The goal of this paper is not to make a precise comparison with observations and find out which galactic model reproduces observations better. The goal is to find out whether image separations can tell us anything about the cosmological models. The key results of this paper are shown in the bottom panels of Figures 9 and 10, and described in §5.2.2. The important thing to realize is that these results are comparative. The main conclusion of this paper is based on the fact that the distributions of image separations are similar in the bottom panel of Figure 9, and identical in the bottom panel of Figure 10. If we had used different galactic models, these curves would probably have been different. However, the *relationship* between these curves would most likely be the same: The distributions would still be similar in Figure 9, and nearly identical in Figure 10. The reason is that these relationships are determined essentially by the properties of the angular diameter distance ratios and their dependence on redshift, as plotted in Figures 7 and 11. Hence, the particular choice of galactic models is not critical, and as long as these models are reasonable, the conclusions remain valid.

6.2. Isolated galaxies

The formulae we use for the angular cross section and image separations (eqs. [6]–[10]) were derived for an isolated nonsingular isothermal sphere. In this paper, we apply these results to our galaxies, assuming that each galaxy acts as if it was alone. When we treat a galaxy as "isolated," we are neglecting both the presence of nearby galaxies and the presence of background matter, that would be present if the galaxy is part of a cluster.

The effect of nearby galaxies is likely be small, for 2 reasons: (1) Even in the center of dense clusters, the number density of galaxies is sufficiently small that having 2 galaxies along a given line of sight is unlikely (see Fig. 10 of Paper II), and if galaxies are off the line of sight, their tidal influence drops rapidly. (2) The most massive galaxies are the ones usually responsible for lensing. The galaxies located near one of these massive galaxies are then presumably much less massive, and their effect would be at most a small correction.

The background matter is a more tricky issue. TOG addressed this issue, and derived an estimate of the effect (their equation [2.36] and [2.37]), but give some words of caution in their Appendix. If the lensing galaxy is located in the center of a dense cluster, the presence of the cluster would increase the image separation. However, the regions located immediately in front of or behind the cluster would presumably be underdense, and their presence would partly compensate the effect of the cluster. Still, we were quite concerned about the possible effect of the background matter. This is why we performed the "no-background" ray-tracing experiments described in §3. These experiments reveal that the effect of the background matter on the distribution of magnifications can be very important (see Fig. 2), but the effect on the distribution of image separations is quite small (see Fig. 1), a spreading of the high-separation tail toward higher values, which is similar in all models and therefore does not affect the comparison between the models. This extent of the high-separation tail of the distribution toward higher separations can explain observed lenses with separations larger than $6''$ (Q0957+561 and J0921+4529). Since the main conclusion of the paper is based on overall comparisons between distributions, it is not affected by the statistics of such rare, very-high-separation cases.

6.3. Source Size

In our analytical model, we correct the angular cross section to account for the finite size of the source [eq. (9)]. Throughout this paper, we assume a fixed source size of diameter $2\alpha_S = 1''$. We introduced the source size in the model after finding a discrepancy between the analytical results and the ray-tracing experiments. Since these experiments all assumed a source size of $1''$, we introduced it in the model, and found out that the numbers listed in Table 4 were in good agreement when the parameter ζ was set to 0.5.

Hence, the source size was introduced merely to demonstrate that the numerical experiments and the analytical model were not in conflict. But from a theoretical viewpoint, it is interesting to have a model which takes the source size into account, and one is always free to set it to zero afterward. Alternatively, the analytical model does not require sources to have all the same size, and a distribution of source sizes could be used instead. Changing the source size (or neglecting it) would modify the various distributions of image separations, but not their relationships with each others, and therefore would not affect the conclusion.

7. SUMMARY AND CONCLUSION

We have designed a simple analytical model to study the distribution of images separations caused by gravitational lensing. Our approach differs from previous work in that we use a galactic model in which the radial density profile has a finite core, while most other studies assume singular density profiles, either singular isothermal spheres, NFW profiles, or point masses. In addition, our model considers the finite angular size of the sources. This has two effects. First, the finite size of the sources introduces an observational selection effect. Individual images cannot be resolved if their separation is less than the angular radius of the unlensed source. Second, the finite size of the sources increases the effective cross section for multiple imaging. A key assumption of our model is that lensing is caused by galaxies only, and the presence of the background matter can be ignored. To test the validity of this assumption, we performed a series of ray-tracing experiments, using the multiple lens-plane algorithm described in Paper I. Our results are the following:

(1) The presence of the background matter tends to increase the image separations produced by lensing galaxies. The peak of the distribution is lowered, the distribution becomes wider, and often develops a high-separation tail. However, this effect is rather small, of order 10%. Furthermore, this effect appears to be independent of the cosmological model. We considered three very different cosmological models: an open, low-density model, a flat, cosmological-constant model, and an Einstein-de sitter model, and found that the effect of the background matter on the distribution of image separation is essentially the same for all models. The effect is always small, and it is therefore correct to ignore the presence of the background matter in our analytical model.

(2) Simulations with galaxies and background matter often produce a secondary peak in the distribution of image separations at large separations, as we noticed previously in Paper II. This peak does not appear in simulations which only include the effect of galaxies, and therefore results from some coupling effect between the galaxies and the background matter.

(3) The effect of the background matter on the magnification distribution is strongly dependent on the cosmological model. This effect is completely negligible in low density models with small density contrast ($\Omega_0 = 0.2$, $\sigma_8 = 0.4$), but becomes very important in models with larger Ω_0 and σ_8 increase, resulting in a significant widening of the distribution. We speculate that the absence of any effect of the background matter in the low-density models results from a cancellation of the density fluctuations along the line of sight, which does not occur (or only to a lesser extend) in cosmological models with higher Ω_0 . We will investigate this problem in more detail in a forthcoming paper.

(4) Nearly all multiple images are caused by early-type galaxies (ellipticals and S0's). The contribution of spiral galaxies to the distribution of image separations is totally negligible. The dominance of early-type galaxies over spirals is an old result that has been pointed out by several authors. Notice, however, that in all studies that assume a galactic model with a singular density profile, the only reason why early-types dominate is because of their larger masses. In our study, galaxies have a finite-density core, and the difference in core radii between early-types and spirals not only reinforces the dominance of early-types, but this effect is even more important than the effect of the mass difference. Furthermore, imposing an observational selection effect based on the finite size of the source (eq. [5]) eliminates about 50% of the multiple images produced by early type galaxies, but more than 95% of the ones produced by spirals.

Of course this is only valid within the assumptions of the analytical model. There are 3 known lenses caused by spiral galaxies (JVAS B0318+357, CLASS B1600+434, and Q2237+030), or about 5% of the total number of observed lenses. The analytical model assumes a one-to-one correspondence between core radius and luminosity, while in the real universe there must be a distribution of core radii at any given luminosity. These three lenses must be spiral galaxies with particularly small core radii.

(5) Without the assumption of a finite source size, our analytical model would have no free parameter. The finite size of the source enters in the model in two different ways. First, it introduces an observational

selection effect, described in terms of a probability $P(s)$ of resolving individually two images separated by an angle s . Second, it increases the effective cross section for multiple imaging by a galaxy. Each one of these effects introduces a free parameter in the model: f in equation (5), which fixes the maximum separation above which two images can always be resolved individually, and ζ in equation (9), which measures the increase in the cross section for multiple-imaging.¹³ By fitting our analytical model to the results of the ray-tracing experiments presented in Paper II, we found that with the particular combination $f = 2$, $\zeta = 0.5$, our analytical model successfully reproduces the distributions of image separations, and also the multiple-image probability, for all cosmological models considered in this paper.

(6) The analytical model predicts that the distributions of image separations are virtually indistinguishable for flat, cosmological constant models ($\Omega_0 + \lambda_0 = 1$) with different values of Ω_0 . For models without a cosmological constant, the distributions of image separations does depend upon Ω_0 , but this dependence is weak. Using the dependence of the image separation and the multiple-imaging cross section on the angular diameter distances, we have come out with a tentative explanation for these results, but this issue probably needs more investigation.

We have considered 7 very different cosmological models, and found that these models produce distributions of image separations that are extremely similar. The largest difference is illustrated in the bottom panel of Figure 9. We conclude that while the number of multiple-imaged sources can put strong constraints on the cosmological parameters (see, e.g., Fox & Pen 2001), the distribution of image separations does not constrain the cosmological models in any significant way, and mostly provides constraints on the structure of the galaxies responsible for lensing.

We have assumed throughout this paper a fixed source redshift $z_S = 3$ and a fixed source angular diameter $2\alpha_S = 1''$. The source size determines the location of the peak in the distribution of image separations. By allowing the source sizes and/or source redshifts to vary, we could modify the shape of the distributions of image separations, especially at small separations. However, these distributions would certainly remain nearly independent of the cosmological model, which is the main result of this paper. Hence, we do not believe that the assumptions of fixed source size and source redshift limit the validity of our results.

We are thankful to Karl Gebhardt for stimulating discussions. This work was supported by Grant 3658-0624-1999 from the Texas Advanced Research Program, NASA Grants NAG5-10825 and NAG5-10826, and Grants NSF ACI 9982297, NSF PHY 0102204, and NPACI NSF UCSD 10181410. PP is very grateful to Rachel Webster and the astrophysics group at the University of Melbourne for the hospitality and fruitful discussion.

REFERENCES

Bernstein, G., & Fischer, P. 1999, AJ, 118, 14
 Blandford, R. D., & Kochanek, C. S. 1987, ApJ, 321, 658
 Burkert, A., & Silk, J. 1999, in Dark Matter in Astrophysics and Particle Physics, Proceedings of the second International Conference on Dark Matter in Astrophysics and Particle Physics, eds. H. V. Klapdor-Kleingrothaus and L. Baudis (Philadelphia: Institute of Physics Publishers), p. 375
 Cheng, Y.-C. N., & Krauss, L. M. 1999, ApJ, 514, 25
 Cole, S., & Lacey, C. 1996, MNRAS, 281, 716
 Dressler, A. 1980, ApJ, 236, 351
 Dyer, C. C. 1984, ApJ, 287, 26
 Efstathiou, G., Ellis, R. S., & Peterson, B. A. 1988, MNRAS, 232, 431
 El-Zant, A., Shlosman, I., & Hoffman, Y. 2001, ApJ, 560, 636
 Fox, D. C., & Pen, U.-L. 2001, ApJ, 546, 35
 Fukushige, T., & Makino, J. 1997, ApJ, 477, L9
 Fukushige, T., & Makino, J. 2001a, ApJ, 557, 533
 Fukushige, T., & Makino, J. 2001b, preprint (astro-ph/0108014)

¹³ Notice that α_S in eq. [5], the source angular radius, is not a free parameter, but a value that must be chosen *a priori*, just like the cosmological parameters Ω_0 and λ_0 , or the parameters in the galaxy luminosity function.

Gebhardt, K. et al. 1996, AJ, 112, 1

Ghigna, S., Moore, B., Governato, F., Lake, G., Quinn, T., & Stadel, J. 2000, ApJ, 544, 616

Hinshaw, G., & Krauss, L. M. 1987, ApJ, 320, 468

Huss, A., Jain, B., & Steinmetz, M. 1999, MNRAS, 308, 1011

Jaroszyński, M. 1991, MNRAS, 249, 430

Jaroszyński, M. 1992, MNRAS, 255, 655

Jing, Y., & Suto, Y. 2000, ApJ, 526, L69

Keeton, C. R. 2001, ApJ, 561, 46

Keeton, C. R., Christlein, D., & Zabludoff, A. I. 2000, ApJ, 545, 129

Klypin, A., Kravtsov, A. V., Bullock, J. S., & Primack, J. R. 2000, preprint (astro-ph/0006343)

Kochanek, C. S. 1995, ApJ, 453, 545

Kochanek, C. S., & Blandford, R. D. 1987, ApJ, 321, 676

Kochanek, C. S., Falco, E. E., Impey, C., Lehár, J., McLeod, B., & Rix, H.-W. 1998, CASTLES Gravitational Lens Database (Cambridge: CfA)

Kravtsov, A. V., Klypin, A. A., Bullock, J. S., & Primack, J. R. 1998, ApJ, 502, 48

Lauer, T. R. et al. 1995, AJ, 110, 6

Li, L.-X., & Ostriker, J. P. 2001, preprint (astro-ph/0010432)

Moore, B., Governato, F., Quinn, T., Stadel, J., & Lake, G. 1998, ApJ, 409, L5

Moore, B., Quinn, T., Governato, F., Stadel, J., & Lake, G. 1999, MNRAS, 310, 1147

Muñoz, J. A. et al. 2001, ApJ, 546, 769

Narayan, R., & White, S. D. M. 1988, MNRAS, 231, 97p

Navarro, J. F., Frenk, C. S., & White, S. D. M. 1996, ApJ, 462, 563

Navarro, J. F., Frenk, C. S., & White, S. D. M. 1997, ApJ, 490, 493

Paczyński, B., & Wambsganss, J. 1989, ApJ, 337, 581

Porciani, C., & Madau, P. 2000, ApJ, 532, 679

Postman, M., & Geller, M. J. 1984, ApJ, 281, 95

Premadi, P., Martel, H., & Matzner, R. 1998, ApJ, 493, 10 (Paper I)

Premadi, P., Martel, H., Matzner, R., & Futamase, T. 2001, ApJ Suppl., 135, 7 (Paper II)

Primack, J. R., Bullock, J. S., Klypin, A. A., & Kravtsov, A. V. 1999, in Galaxy Dynamics, eds. by D. R. Merritt, M. Valluri, and J. A. Sellwood, ASP Conference Series vol. 182 (San Francisco: ASP)

Romanowsky, A. J., & Kochanek, C. S. 1999, ApJ, 516, 18

Rusin, D. & Ma, C.-P. 2001, ApJ, 549, L33

Schneider, P., Ehlers, J., & Falco, E. E. 1992, Gravitational Lenses (New York: Springer) (SEF)

Shapiro, P. R., Iliev, I. T., & Raga, A. C. 1999, MNRAS, 307, 203

Spergel, D. N., & Steinhardt, P. J. 1996, Phys.Rev.Lett., 84, 3760

Tormen, G. , Bouchet, F. R., & White, S. D. M. 1997, MNRAS, 286, 865

Takahashi, R., & Chiba, T. 2001, preprint (astro-ph/0106176)

Turner, E. L., Ostriker, J. P., & Gott, J. R. 1984, ApJ, 284, 1 (TOG)

Tyson, J. A., Kochanski, G. P., & Dell'Antonio, I. P. 1998, ApJ, 498, L107

Walsh, D., Carswell, R. F., & Weymann, R. J. 1979, Nature, 279, 381

Young, P., Gunn, J. E., Kristian, J., Oke, B., & Westphal, J. A. 1980, ApJ, 241, 507